Nano Research

Open Access

Research Article

Anisotropic resistive switching of 2D-layered single crystal halide perovskite $CsPb_2Br_5$-based memristor

Uijin Jung[1], Dae-Seong Woo[2], Sangmin Kim[1], Zhaozhong Tan[1], and Jinsub Park[1,2,3] ✉

[1] *Department of Electronic Engineering, Hanyang University, Seoul 04763, Republic of Korea*
[2] *Department of Nanoscale Semiconductor Engineering, Hanyang University, Seoul 04763, Republic of Korea*
[3] *Department of Semiconductor Engineering, Hanyang University, Seoul 04763, Republic of Korea*

Cite this article: *Nano Research*, **2025**, *18*, 94907023. https://doi.org/10.26599/NR.2025.94907023

ABSTRACT: Metal halide perovskites (MHPs) have attracted attention in advanced memory technology, such as resistive switching (RS) devices, owing to their hysteretic behavior. However, the mechanisms underlying MHP-based RS devices remain elusive. We present a two-dimensional (2D)-layered single-crystal (SC) $CsPb_2Br_5$ microsheet-based RS device with vertical and planar structures. Although RS occurs in both structural devices, the planar structured device exhibits volatile RS operation, whereas the vertically structured device exhibits bipolar RS characteristics, including a long retention time (> 2.5 × 10^4 s), large on/off ratio (up to 10^8), low-operating voltage (V_{set} < 0.32 V), and reset voltage-driven multilevel properties with a large resistance ratio (~ 10^2) between each state. A possible RS mechanism of the vertically structured devices can be explained by the migration of active metal ions. The 2D-layered structure induces partial localization of active metal elements between the Cs layers owing to its high migration barrier energy level along the [001] crystal direction. Experimental and theoretical analyses, including Auger electron spectroscopy depth-profile and density functional theory calculations support our suggestions. This work clarifies the operational mechanisms in SC MHP-based anisotropic RS and proposes the potential for SC MHP in advanced memory devices, marking a leap in the understanding and application of these materials for next-generation electronics.

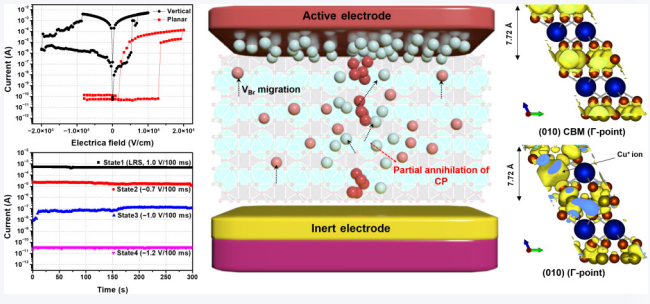

KEYWORDS: halide perovskite, single crystal, resistive switching, ion migration, two-dimensional material

1 Introduction

Resistive switching (RS) memory has been in the spotlight for the last decades as a candidate for next-generation non-volatile memory and computing systems owing to its fast-switching speed, low power consumption, superior scalability, and high integration density [1–3]. In particular, in the past several years, RS memory devices have been investigated not only by theoretical and experimental analysis of the RS phenomenon itself, but also adopted in memristors, synaptic components, and in-memory computing systems with remarkable performances [1, 4]. Among the previously reported active materials such as metal oxides, organics, and metal halide perovskites (MHPs) for RS memory devices, inorganic MHPs have recently received attention as excellent candidates for RS devices owing to their high order on/off ratio, low operating power consumption, and better environmental stability compared to organic MHPs [5–7]. Since Wu et al. first reported the all-inorganic $CsPbBr_3$-based RS device in 2016, numerous related studies have been conducted [7–9]. However, its superiority such as a high device performance with low-power consumption and a facile fabrication process, relatively limited on/off ratio and vulnerability to humidity and heat is the main challenges to be addressed [10, 11]. Decreasing the dimensions of the MHP structure was considered an emerging approach to improving the limitations, which are inherent properties in three-dimensional (3D) MHP-based devices owing to their large bandgap and better environmental robustness compared to 3D MHP [12, 13]. In 2020, Jung et al. newly presented polycrystalline $CsPb_2Br_5$ film-based RS devices with a higher on/off ratio and stability than the $CsPbBr_3$ film, and Paul et al. suggested $CsPb_2Br_5$ nanoplates-based flexible RS devices with light-modulated multilevel functions [13, 14]. However, single-crystal (SC) $CsPb_2Br_5$ without grain-boundary (GB)-based RS devices have never been reported, although the existence of the GB in the MHP film could directly

Received: May 6, 2024; **Revised:** July 30, 2024
Accepted: September 4, 2024

✉Address correspondence to jinsubpark@hanyang.ac.kr

influence the RS characteristics of the devices. The GB present in the MHP could facilitate the migration of active metal and mobile defect ions that could cause RS, as well as inferior device-to-device reliability, easier degradation caused by environmental stress, and a large current flow in the high-resistance state (HRS), resulting in a limited on/off ratio [15–17]. Moreover, the RS characteristics resulting from the presence of a large number of GBs could hide the characteristics of the MHP material itself, thereby canceling out the unique characteristics inherent in the MHP material [17, 18].

In this study, we first evaluated the performance of GB-free two-dimensional (2D)-layered $CsPb_2Br_5$ microsheet (MS)-based RS devices, which exhibited a high on/off ratio of up to approximately 10^8, an extended data retention time ($> 2.5 \times 10^4$ s), a low-operating voltage ($V_{set} < 0.32$ V), and a multilevel function with a large resistance margin (~ 10^2) between each state. The RS behavior of the $CsPb_2Br_5$-based RS devices exhibited a significant dependence on the planar and vertical-type structures. This discrepancy in the device structures stems from the distinct mobile-ion migration characteristics associated with the crystal plane of $CsPb_2Br_5$. This result was drawn from the results of the Auger electron spectroscopy (AES) in conjunction with the electrical characteristics of the fabricated devices. Density functional theory (DFT) calculations, including the climbing image nudged elastic band (CI-NEB) method, further supported this observation.

2 Results and discussion

The crystal structure of the tetragonal $CsPb_2Br_5$ obtained using the VESTA software (ver. 3.5.8) is shown in Fig. 1(a), which depicts a Pb_2Br_5 polyhedron spaced by a Cs atom layer. Consequently, tetragonal $CsPb_2Br_5$ was classified as a 2D structural material [19–21]. We successfully synthesized SC 2D-layered $CsPb_2Br_5$ MS by a facile solution-based fractional crystallization technique according to the synthesis process shown in Fig. S1 in the Electronic Supplementary Material (ESM). The measured X-ray diffraction (XRD) pattern of the precipitated sheet-type powder during the crystallization process corresponded well with the calculated results from the SC crystallographic data and the reported tetragonal $CsPb_2Br_5$ structures (JCPDS No. 25-0211), as displayed in Fig. 1(b) [20, 21]. The main peaks appeared at 11.88°, 23.61°, 35.62°, 48.04°, and 48.22° and corresponded to the $CsPb_2Br_5$ crystal planes of (002), (210), (312), (413), and (420), respectively.

However, the precipitated powder may contain overgrown and excess precursor material; therefore, it contains some of the other Cs-Pb-Br family compounds, such as $CsPbBr_3$, Cs_4PbBr_6, $PbBr_2$, and CsBr [21, 22]. To use only pure $CsPb_2Br_5$ crystals for high-quality RS devices, the growing precursor solution in the metastable zone was dropped on the target substrate, as described in the experimental section. After a few minutes, sheets of hundreds of micrometers became visible to the naked eye, and at this point, the solution was temporarily removed to abruptly stop growth. scanning electron microscopy (SEM) and energy dispersive spectroscopy (EDS) analyses were performed to evaluate the composition and surface of the $CsPb_2Br_5$ MSs grown in this manner. As shown in Fig. 2(a), the synthesized MS displayed a remarkably smooth edge and surface, free from any undesired composites, despite the easy formation of Cs-Pb-Br composites at the edges of the $CsPb_2Br_5$ MSs [23]. The atomic elements ratio measured by EDS analysis (Fig. 2(b)) was 1:2.03:4.92 (Cs:Pb:Br) whose values nearly corresponded with the stoichiometric atomic ratio of $CsPb_2Br_5$. In addition, it can be observed from the EDS mapping results that Cs-Pb-Br elements were uniformly present throughout the MS. For a more accurate confirmation, typical appropriately grown MS was separated and transferred to a holey-carbon Cu grid for transmission electron microscopy (TEM) analysis. As shown in Fig. 2(c), the smooth surface of the MS in the high-resolution (HR)TEM images indicated that there was no other material with a different phase on the surface of the material. Moreover, the interplanar spacings 2.99 and 2.71 Å obtained from the HRTEM image and selected area diffraction (SAED) pattern corresponded to (220) and (310) interplanar spacings, respectively, which indicated that the synthesized material was tetragonal $CsPb_2Br_5$. Moreover, the consistent repetition of a specific diffraction pattern in the SAED pattern indicated that the synthesized materials exhibited an SC structure, as shown in Fig. 2(e). It should be noted that the edges of the synthesized SC $CsPb_2Br_5$ MS coincided with the [100] or [110] directions, as depicted in Fig. 2(d) and Fig. S2 in the ESM. Furthermore, the lattice parameters a and b of the tetragonal $CsPb_2Br_5$ MS were same, which indicated that the direction perpendicular to the plane of the synthesized SC $CsPb_2Br_5$ MS was parallel to the [001] direction (in particular, (002)-oriented) [21]. To further analyze the crystalline quality of the SC $CsPb_2Br_5$ MS, the X-ray rocking curve (XRC) of the (002) plane was measured, as depicted in Fig. 2(f). The

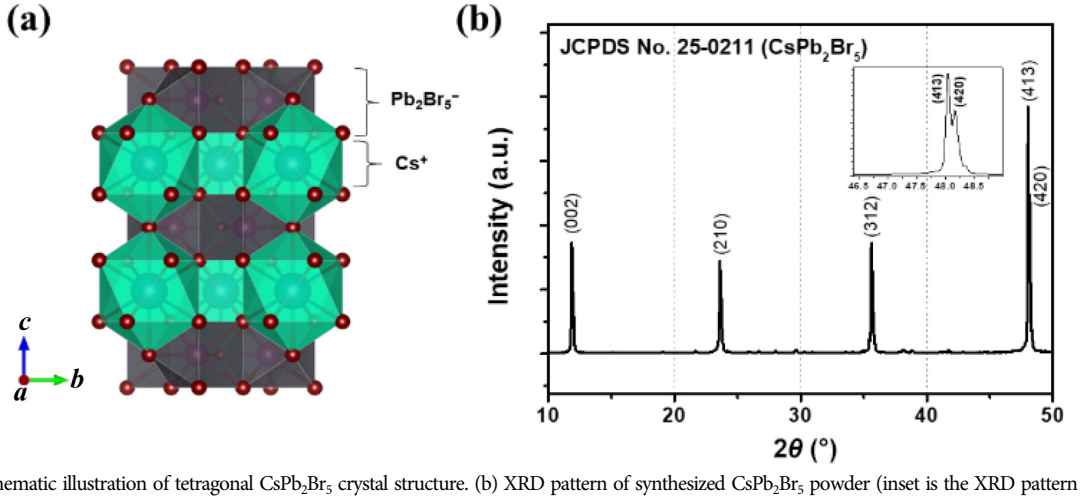

Figure 1 (a) Schematic illustration of tetragonal $CsPb_2Br_5$ crystal structure. (b) XRD pattern of synthesized $CsPb_2Br_5$ powder (inset is the XRD pattern of the enlarged magnification at approximately 48°).

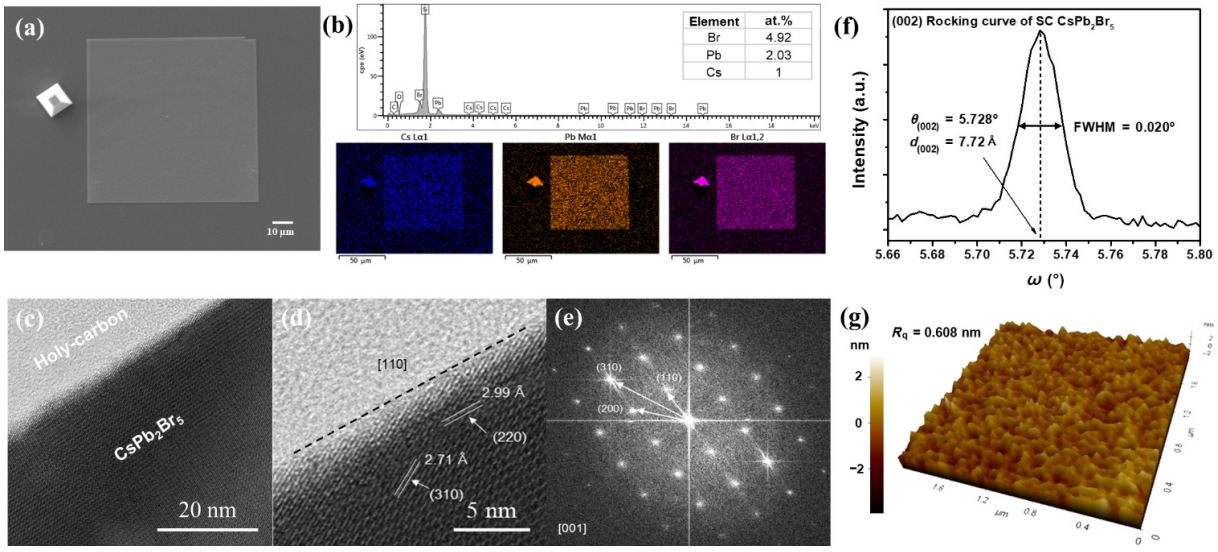

Figure 2 (a) Typical SEM image and (b) EDS mapping results of $CsPb_2Br_5$ MS on SiO_2/Si substrate (Inset presents the elemental atomic ratio measured by EDS-SEM). (c) and (d) HRTEM images of $CsPb_2Br_5$ edge and (e) SAED pattern obtained fast Fourier transforms (FFT) technique from HRTEM image of (c). (f) XRC and (g) AFM results of SC $CsPb_2Br_5$ single MS on SiO_2/Si substrate.

measured full width at half maximum (FWHM) of the (002) peak of the rocking curve is as small as 0.020°. The small FWHM value in the (002) peak of the rocking curve confirms that the synthesized $CsPb_2Br_5$ on the substrate is (002)-oriented, and also indicates that it is a high-quality crystal with negligible residual stress [22, 23]. Atomic force microscopy (AFM) analysis was conducted to determine the surface roughness and atomic steps of the SC $CsPb_2Br_5$ MS. As shown in Fig. 2(g), the root mean square roughness (R_q) of the SC $CsPb_2Br_5$ MS surface on the substrate is approximately 0.608 nm, indicating a very uniform surface. Additionally, given that the (002) interplanar distance of the synthesized $CsPb_2Br_5$ crystal is 7.72 Å which can be calculated from (002) peak of 5.732°. Based on this, the R_q value of 0.608 nm suggests that the surface of CsPb2Br5 MS is highly uniform, with deviations occurring only at the level of a single Cs^+ and $Pb_2Br_5^-$ layer.

RS devices with vertical and planar structures were designed to evaluate the anisotropic RS characteristics of $CsPb_2Br_5$ according to their crystal direction, which is not observable in polycrystalline devices. First, to fabricate a vertical-type RS device, as depicted in Fig. 3(a), the $CsPb_2Br_5$ MS was grown on a pre-patterned Au bottom electrode (BE) formed on Al_2O_3(0001) substrate using the same method mentioned above, and the Au or Cu top electrode (TE) was deposited by thermal evaporation, as explained in Fig. S3 in the ESM. A cross-sectional SEM image of a typical fabricated device is shown in Fig. 3(b), where each layer of the RS device is clearly distinct. The measured thickness of the $CsPb_2Br_5$ MS from the cross-sectional SEM image is approximately 500 nm. As with the previous crystallographic analysis results, including the XRD and TEM measurements, because the synthesized $CsPb_2Br_5$ was an SC, it did not exhibit a distinct GB, unlike the halide perovskite films formed by generally used spin coating, blade coating, and thermal evaporation techniques [24, 25, 26]. The inset of Fig. 3(b) shows an optical microscopy (OM) image of the fabricated Au/$CsPb_2Br_5$/Cu structure and the white dotted box indicates the actual active region of the RS device. To confirm the absence of impurities in the $CsPb_2Br_5$ MS used in a typical device, micro-Raman spectroscopy was conducted around the active region (not the inner active layer to prevent laser damage) of the $CsPb_2Br_5$ MS, as shown in Fig. 3(c). The observed Raman shift peaks at 51, 69, 76, and 134 cm^{-1} are in accordance with previous reports of the Raman shift of $CsPb_2Br_5$ [20, 27]. The peaks located at 51 and 134 cm^{-1} are from the A_{1g} vibration mode and the peaks located at 69 and 76 cm^{-1} are from the B_{2g} and B_{1g} vibration mode, respectively. These results confirmed once again that $CsPb_2Br_5$ used as an active region, does not contain unwanted Cs-Pb-Br compounds.

The electrical properties of the devices with inert and active metal electrodes were measured to understand the RS characteristics of the fabricated vertical-type device. In devices using inert Au TE, there is a possibility that the resistance can be changed

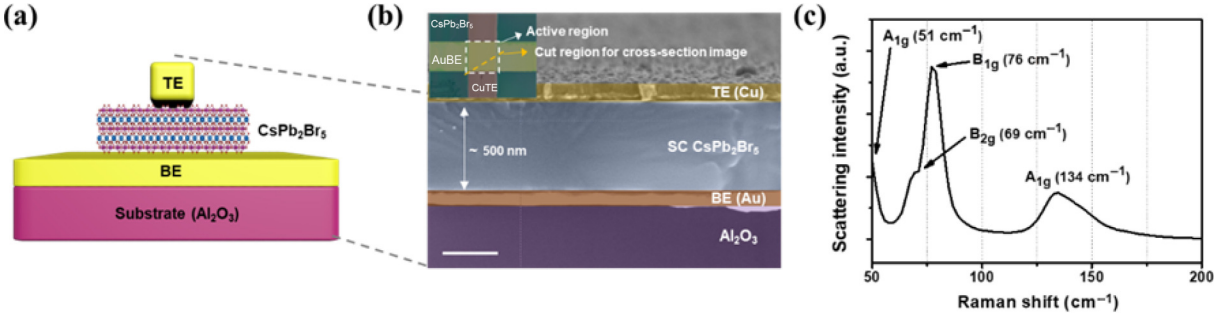

Figure 3 (a) Schematic illustration of fabricated vertical-type RS device and (b) typical cross-section SEM image of actual RS device (inset is OM image of typical fabricated vertical-type device). (c) Raman shift of $CsPb_2Br_5$ MS for actual active area in RS device.

only by the migration of mobile defect ions inside $CsPb_2Br_5$ MS. In general, among the defect ions in the $CsPb_2Br_5$ crystal, the bromine vacancy (V_{Br}) was considered the most dominantly formed mobile defect owing to its lowest formation energy compared to other ion vacancies in the $CsPb_2Br_5$ crystal [13, 28]. It is noteworthy that the RS device with the Au TE did not exhibit any significant RS behavior even in high voltage conditions up to ± 9 V bias as shown in Fig. 4(a). This result is the opposite of the results reported on the polycrystalline $CsPb_2Br_5$-based RS device, which exhibited apparent RS characteristics; this implies that the vertical direction (perpendicular to (001) plane) migration of defects such as V_{Br} in $CsPb_2Br_5$ were significantly restricted in GB-free SC $CsPb_2Br_5$ [13]. However, as depicted in Fig. 4(b), when an active metal Cu was used as a TE, a clear bipolar RS phenomenon appeared after the electrochemical forming process at 2.0 V (Fig. S4 in the ESM), and the RS characteristics were maintained for approximately 100 loop cycles. Almost the same current–voltage (I–V) characteristics were observed in different devices with identical $CsPb_2Br_5$ thicknesses fabricated in the same manner, as shown in Fig. S5 in the ESM. As demonstrated in Fig. S6 in the ESM, the bipolar RS characteristic of the fabricated SC $CsPb_2Br_5$-based RS device can be maintained for 5 weeks under an air atmosphere without any passivation layer. This result demonstrates that the environmental stability of the fabricated SC $CsPb_2Br_5$ is superior to polycrystalline MHP-based RS devices [8, 15]. This enhanced stability is likely due to the absence of grain boundaries, which are the primary degradation paths in polycrystalline MHP [16]. On the other hands, a device with an Ag TE instead of a Cu TE was fabricated, demonstrating similar bipolar non-volatile RS characteristics, as shown in Fig. S7 in the ESM. However, it exhibited relatively high voltage requirements for set and reset with unstable RS loop characteristics compared to the device using a Cu TE. These findings led to the employment of Cu TE in SC $CsPb_2Br_5$-based RS devices. The voltage required to transition from the HRS to the low-resistance state (LRS) was referred to as V_{SET} and the voltage required to transition from the LRS to the HRS was V_{RESET}; the distributions of V_{SET} and V_{RESET} are illustrated by a histogram with the Gaussian fitting in Fig. 4(c). The calculated average V_{SET} and V_{RESET} of the fabricated $CsPb_2Br_5$-based vertical-type RS device are approximately 0.32 and –0.80 V, respectively, which are appropriate for applying a low-power consumption system. The retention times of the fabricated $CsPb_2Br_5$-based vertical-type RS device when 500 ms voltage pulses of 0.4 and –1.0 V were applied were evaluated using a reading voltage of 0.05 V (10 ms). The obtained results suggested that the resistance in the LRS and HRS could be sustained without notable degradation for a minimum duration of 2.5×10^4 s, as shown in Fig. 4(d), which indicates the non-volatile characteristics inherent in the fabricated SC $CsPb_2Br_5$ MS-based vertical-type RS device. Furthermore, as depicted in Fig. S8 in the ESM, extrapolating the LRS current on a logarithmic scale to the logarithmic time axis indicates that the LRS current level could be retained for 10 years. In contrast, the HRS resistance varied for each loop, as depicted in Fig. 4(b) and Fig. S5 in the ESM. To evaluate this result in detail, the LRS and HRS resistances at 0.05 V were extracted from the I–V loops, as shown in Fig. 4(b). The sweep cycle endurance extracted from the I–V loops, as shown in Fig. 4(e), exhibited a significantly large fluctuation in the HRS resistance, whereas the LRS resistance could be retained at a similar level. The diverse HRS resistance and continuous distinct negative differential resistance (NDR), which could be observed in the I–V characteristics in Fig. 4(b), indicates that the SC $CsPb_2Br_5$ MS-based vertical-type RS devices may have multiple HRS states that can be managed by different voltage biases. Based on these observations, we evaluated the multistate transition characteristics based on the amplitude of the reset voltage pulse.

Figure 4(f) shows the cycle endurance of the reset voltage-driven multistate operation, confirming reproducible transition from LRS (state1) to HRS1 (state2), HRS2 (state3), and HRS3 (state4) by applied voltage pulses of –0.7, –1.0, and –1.2 V (100 ms), respectively. Additionally, each of the four states could maintain a resistance level for at least 300 s without any degradation, with a large on/off ratio of approximately 10^2 as shown in Fig. 4(g). This multistate operation with a large on/off resistance ratio between each state, which could be controlled only by the voltage, could accelerate practical applications by reducing the need for an additive-specific circuit for multistate operation or lowering the complexity of the circuit. Moreover, through the temperature dependence of the resistance in LRS, it is possible to determine whether the component of the conductive path (CP) formed inside the RS layer is metallic or ionic [29–31]. In general, the temperature coefficient of resistance (TCR, α) can be expressed as $R = R_0[1 + \alpha(T - T_0)]$, where R_0 is the resistance at T_0. As depicted in Fig. 4(h), the LRS resistance of the fabricated SC $CsPb_2Br_5$ MS-based vertical-

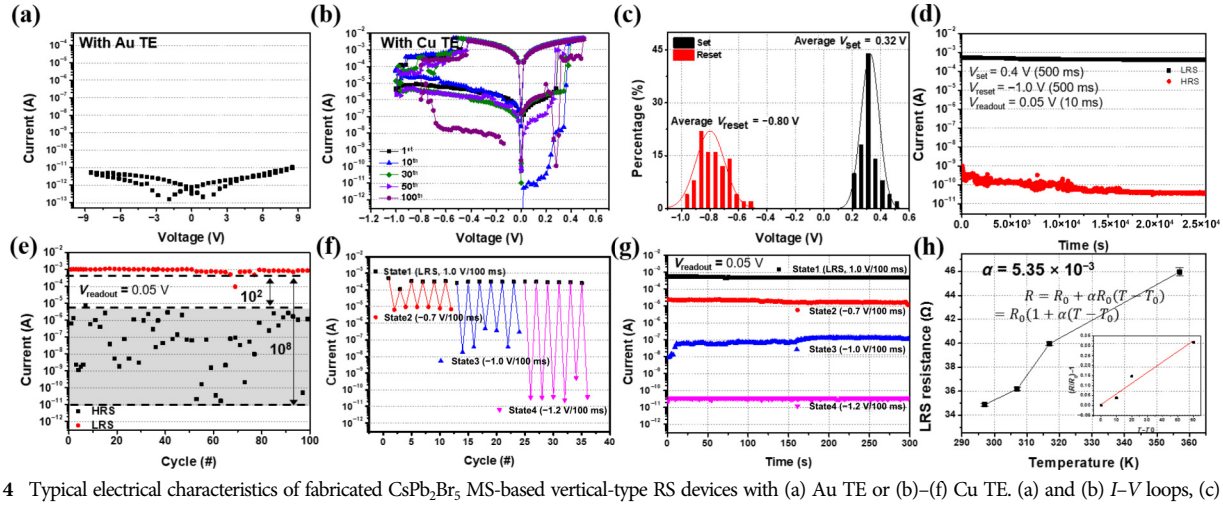

Figure 4 Typical electrical characteristics of fabricated $CsPb_2Br_5$ MS-based vertical-type RS devices with (a) Au TE or (b)–(f) Cu TE. (a) and (b) I–V loops, (c) set and reset voltage distribution, (d) resistance retention time in LRS and HRS, (e) sweep cycle endurance extracted from I–V loops, (f) reset voltage driven multistates cycles endurance, (g) each state retention time, and (h) LRS resistance depending on temperature of fabricated $CsPb_2Br_5$ MS-based vertical-type RS devices.

type device exhibited a positive proportional relationship with the temperature, and the TCR obtained according to the above equation was approximately 5.35 × 10^{-3} 1/K, which was almost consistent with the reported TCR of copper [26, 30]. Furthermore, given the relatively high magnitude of the TCR value in comparison to the typically low TCR of ionic CP (under 2 × 10^{-3} 1/K) [30, 32–34], it is anticipated that the cause of RS in the fabricated SC $CsPb_2Br_5$ MS-based vertical-type RS device was predominantly attributed to copper. A more detailed discussion of the behavior of Cu, which is a component of the CP inside SC $CsPb_2Br_5$ will be discussed in later sections.

To evaluate the anisotropic RS phenomenon of the SC $CsPb_2Br_5$-based RS device, planar-type RS devices with inert (Au) and active metal (Ag) electrodes were fabricated using the fabrication process shown in Fig. S3 in the ESM. The planar-type RS device had an RS active layer of approximately 2 μm in directions parallel to the (001) plane, which was different from the RS active layer thickness of the vertical-type device. Consequently, the measured RS characteristics with the electrical field along the *x*-axis were used for comparative analysis between the two structures. Figure 5(a) compares the *I*–*V* loop characteristics of the SC $CsPb_2Br_5$ MS-based planar and vertical-type RS devices with inert electrodes. As mentioned earlier, in the vertical-type RS device with inert electrodes used as the TE and BE, the RS phenomenon did not occur, even at a high electric field of approximately 180 kV/cm. However, in the planar-type RS device, a clear RS phenomenon occurred, even at a relatively low electric field of 100 kV/cm. This could be attributed to the migration of V_{Br}, which is widely present in $CsPb_2Br_5$ crystals, depending on the electric field. This observation suggests that the migration of V_{Br} is significantly impeded in the vertical direction (perpendicular to the (100) plane), whereas migration in the planar direction (parallel to the (001) plane) is feasible. Nonetheless, the SC $CsPb_2Br_5$-based planar-type RS device with an inert electrode exhibits volatile RS characteristics. Figure 5(b) shows the *I*–*V* loop characteristics of the SC $CsPb_2Br_5$ MS-based vertical- and planar-type RS devices with active electrodes. The planar-type RS device with an active electrode still exhibited volatile RS characteristics, such as when an inert electrode was used, but the set electric field required for the transition from the HRS to LRS was only approximately 13 kV/cm, which was significantly smaller than that of the inert electrode. The collaboration between V_{Br} and the active metal within $CsPb_2Br_5$ suggests that a discernible RS phenomenon is likely to occur even at relatively low electric-field levels. As shown in Fig. 5(c), even after applying a high electric field of 100 kV/cm for the set, the planar-type device had a shorter retention time of 544.9 s compared to the vertical-type device and had volatile memory characteristics. Based on these findings, it is hypothesized that the volatile characteristics observed in planar-type RS devices stem primarily from the crystal structure along the $CsPb_2Br_5$ (001) plane and are independent of the migration behavior of the mobile defects or active metal ions. A more in-depth examination of this phenomenon is discussed in the following section, drawing insights from the DFT and CI-NEB calculation results.

Generally, in vertical-type RS devices, the component of the CP formed from the internal mobile defects or active metal ions from the TE can be affected by the thickness of the active layer, which ultimately affects the RS characteristics [35, 36]. To confirm the changes in the RS characteristics according to the thickness of the SC $CsPb_2Br_5$ active layer, the SC $CsPb_2Br_5$ based vertical-type RS device was fabricated using SC $CsPb_2Br_5$ with a thickness of approximately 110 nm, as shown in the cross-sectional SEM image in Fig. S9 in the ESM, which is much thinner than the previously proposed 500 nm. Figure 6(a) depicts a typical *I*–*V* loop of a thin SC $CsPb_2Br_5$-based vertical-type RS device with an inert top TE. Similar to the device with 500 nm SC $CsPb_2Br_5$, no discernible RS phenomenon was observed according to the electric field. These results indicate that defects like V_{Br} in (002)-oriented $CsPb_2Br_5$ are constrained from moving along the perpendicular to (001) plane, preventing them from forming CPs, regardless of the active layer thickness. However, it is worth noting that the HRS current magnitude of the device was higher than that of the 500 nm SC $CsPb_2Br_5$-based one. This is likely because the resistance increases with the thickness of $CsPb_5Br_5$, serving as the active and resistance layer simultaneously [35–37]. However, as shown in Fig. 6(b), the thin SC $CsPb_5Br_5$-based vertical-type RS device with an active TE exhibited bipolar non-volatile RS characteristics, such as a device with a thickness of 500 nm, and was also confirmed to have different HRS states in the first and second loops. In other words, it was confirmed that there was no significant difference in the migration behavior of the mobile defects or active metal ions according to the thickness of the SC $CsPb_2Br_5$ contrary to the reported results [35, 36]. This phenomenon is attributed to the sustainability of the crystallinity and crystal direction of SC perovskites, regardless of the layer thickness, owing to the absence of grain boundaries.

To determine the exact composition of the CPs, the depth profiles of the LRS and HRS of the fabricated RS devices were measured using AES. The depth profile analysis of the RS layer has often been carried out for the analysis of the RS mechanism by ion migration such as halogen and metal elements; however, AES depth profile analysis of the GB-free SC HP-based RS device was conducted in this study [35, 38]. Ion sputtering for the etching of the sample was performed at an incident angle of 45° for the sample using an Ar^+ ion of 0.5 keV, and AES analysis was conducted by

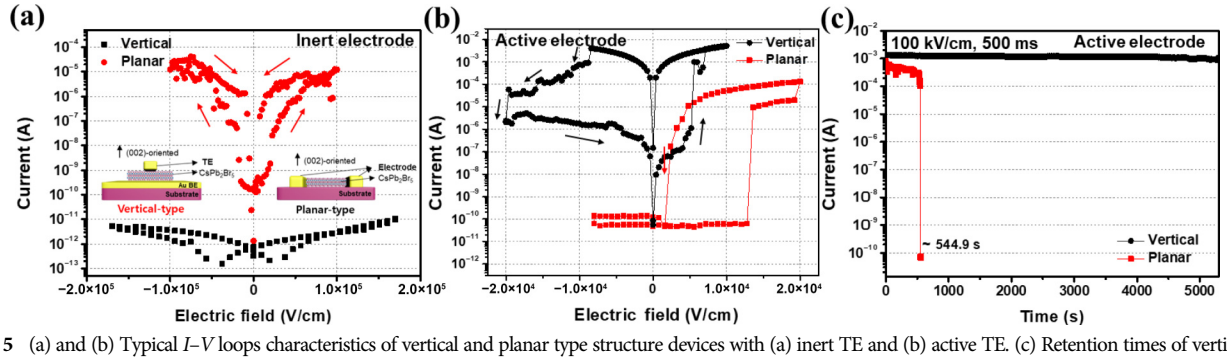

Figure 5 (a) and (b) Typical *I*–*V* loops characteristics of vertical and planar type structure devices with (a) inert TE and (b) active TE. (c) Retention times of vertical and planar type structure devices with active TE.

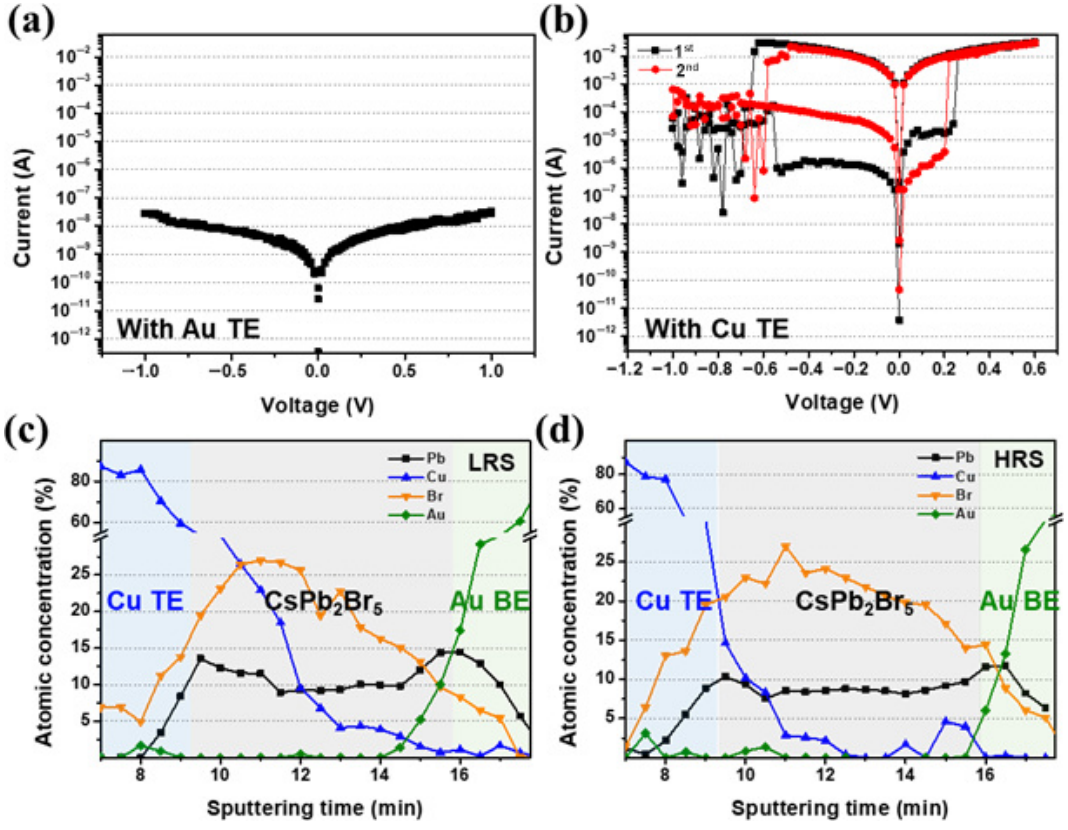

Figure 6 Typical *I*–*V* loops of thin $CsPb_2Br_5$ MS-based vertical-type RS devices with (a) Au and (b) Cu TE. AES depth profiles of thin MS $CsPb_2Br_5$-based vertical-type RS devices with Cu TE in (c) LRS and (d) HRS.

placing an electron gun of 10 keV with 10 nA at a reflection angle of 30° for the sample. The SC $CSsPb_2Br_5$ was found to have an etch rate of approximately 15.7 nm/min under the corresponding ion sputtering conditions. Unfortunately, as shown in Fig. S10 in the ESM, the degradation of SC $CsPb_2Br_5$ was evident in the SEM image captured during ion etching. Electron beam analysis was conducted in the middle of the AES depth profile analysis process of the 500 nm SC $CsPb_2Br_5$-based vertical-type device. In particular, the Auger electron scan area rapidly deteriorated from the two-thirds point owing to the electron beam, thereby compromising the reliability of the AES depth profile analysis of the sample. However, considering that no notable degradation was identified in the SEM image at the A-third point, depth profile analysis using the AES technique on the relatively thin 110 nm SC $CsPb_2Br_5$-based vertical-type device is likely to be reliable. Figures 6(c) and 6(d) show the depth profiles of the thin SC $CsPb_2Br_5$-based vertical-type RS device in the LRS and HRS states, respectively. First, the atomic concentration distribution of the Br atom is slightly higher on the Cu TE layer side in the LRS, which could indicate that the V_{Br}^+ ion has migrated in response to the electric field. However, the distinction of the Br atom concentration distribution between the LRS and HRS has not been clearly delineated. These results imply that V_{Br} ion migration perpendicular to the (001) plane of SC $CsPb_2Br_5$ is undesirable, as expected from the previous *I*–*V* characterization results, even if it cannot form CPs that can cause the RS phenomenon. However, it should be noted that the atomic concentration distribution of Cu varies significantly between the LRS and HRS states. In the LRS state, the atomic concentration of Cu is present with a concentration gradient across the $CsPb_2Br_5$ region, whereas in the HRS state, the atomic concentration of Cu is generally low in the overall $CsPb_2Br_5$ region, and partially absent. This result indicates that the Cu ions may sufficiently migrate in a direction perpendicular to the (001) plane, depending on the direction of the electric field, and the migrated Cu ions are reduced by electrons supplied from the BE to form CPs, which is essential for RS operation [39]. Moreover, the active participation of Cu ions from active TE is also evidenced by the distinct *I*–*V* characteristics and retention performance compared to inert electrodes in Fig. 5. Meanwhile, despite the CPs destruction by the electric field, some Cu element was not completely removed, and remained in the $CsPb_2Br_5$ layer in the HRS. The residual Cu elements in the $CsPb_2Br_5$ layer were not independent of the reset voltage-driven multistate RS operation of the fabricated SC $CsPb_2Br_5$-based vertical-type RS devices.

The behavior of the V_{Br} and Cu ion in the SC $CsPb_2Br_5$ was predicted by calculation through the CI-NEB technique [39, 40]. The Cu^+ and V_{Br}^+ ions were moved inside the $CsPb_2Br_5$ lattice, because Cu and V_{Br} are ionized through redox reactions such as $Cu \rightarrow Cu^+ + e^-$ and $Br \rightarrow V_{Br}^+ + e^-$, the CI-NEB calculation was performed by considering the total charge within the entire system to compensate for the charge generated by the reaction. To predict the migration behavior of Cu^+ ions in the SC $CsPb_2Br_5$ lattice, the migration barrier energy (MBE) was calculated by setting the path as an image that could be moved in directions perpendicular and parallel to the (001) plane within the supercell. As shown in Fig. 7(a), the calculated MBEs of Cu^+ ions perpendicular (black line) and parallel (red line) to the (001) planes are displayed. As mentioned above, it should be noted that $CsPb_2Br_5$ has a 2D-layered structure in which the Cs and Pb_2Br_5 polyhedron layers are repeatedly stacked [19, 20]. When Cu^+ ion moves in a direction perpendicular

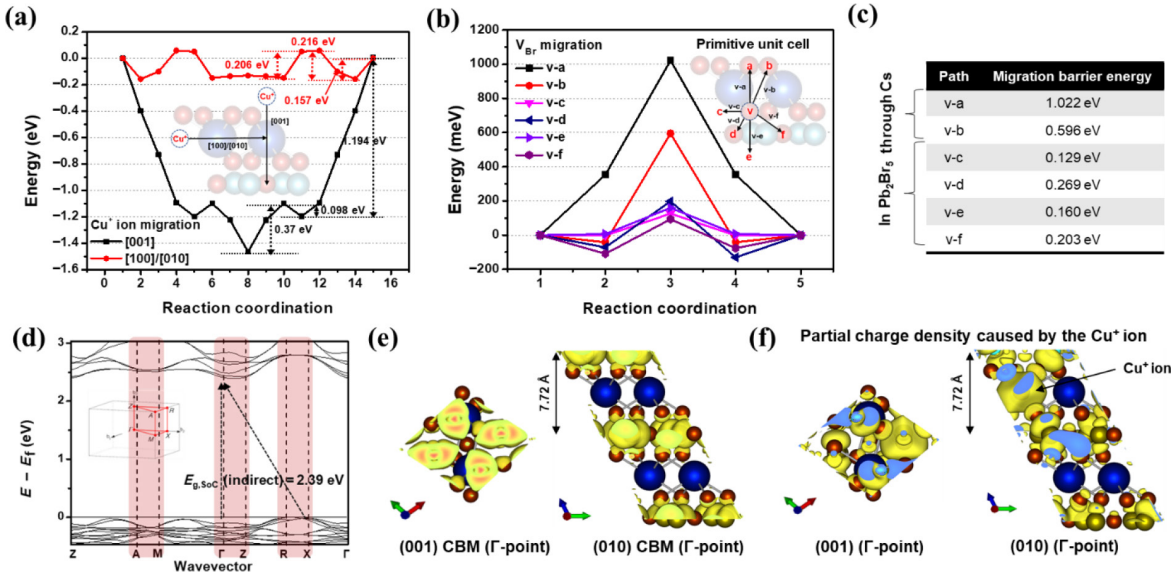

Figure 7 Calculated MBEs of (a) Cu^+ and (b) and (c) V_{Br} ions in the $CsPb_2Br_5$ lattice by CI-NEB method, (b) E-*k* band structure with SOC effect, (e) electron charge density of pristine bulk $CsPb_2Br_5$ crystal at CBM with different viewpoints (001) and (010), and (f) caused by Cu^+ ion in $CsPb_2Br_5$ crystal at the Γ-point.

to the (001) plane, the Cu^+ ion has the lowest energy of the total system energy, which indicates a stable state when passing through the Cs layer. A more detailed description of the positions of the Cu^+ ions is shown in Fig. S11 in the ESM. The MBE increased as it passed through the Pb_2Br_5 polyhedron layer, with an MBE of approximately 1.194 eV when passing through the Pb layer. Meanwhile, to predict the movement of Cu^+ ions in a direction parallel to the (001) plane, the MBE was calculated from the most stable position, as shown above, Cu^+ ion in the Cs layer, to the [100] direction (same as [010] in the tetragonal structure). The red line in Fig. 7(a), representing movement parallel to the (001) plane, significantly differs from the black line, indicating perpendicular movement, and it has a low MBE of up to approximately 0.216 eV. In addition, when there was one V_{Br} in the supercell, the MBEs for the V_{Br}^+ ion migration were meticulously computed based on the direction toward the adjacent atomic positions of Br. As shown in Fig. 7(b), the MBE calculated as v-c (0.129 eV), v-d (0.269 eV), v-e (0.160 eV), and v-f (0.203 eV) within the Pb_2Br_5 polyhedral layer exhibited relatively low values compared to the v–a and v-b paths across the Cs layer of up to 1.022 eV. The calculated low MBEs of both the Cu^+ and V_{Br}^+ ions in the direction parallel to the (001) plane could explain the occurrence of the RS phenomenon regardless of whether the electrodes were inert or active in the SC $CsPb_2Br_5$ based planar-type RS devices. Simultaneously, MBEs as low as approximately 0.157 eV (Cu^+ ion) and 0.217 eV (V_{Br}^+ ion) could cause the thermally activated spontaneous collapse of CPs, regardless of whether the electrode was inert or active, resulting in very short retention times and volatile RS characteristics [41–43]. Whereas appropriately high MBEs of Cu^+ ions migrating perpendicular to the (001) plane can cause non-volatile RS characteristics with an excellent resistance retention capability of the SC $CsPb_2Br_5$-based vertical-type device with active Cu TE, as shown in Fig. 4(d). Almost the same trend was observed when Cu was replaced with Ag and calculated using the same CI-NEB technique as shown in Fig. S12 in the ESM. However, the calculated MBEs were slightly higher than the MBEs of Cu^+ ions, which may be the cause of the V_{SET} and V_{RESET} being slightly higher than the use of Cu TE in SC $CsPb_2Br_5$ based qualitative-type devices with Ag TE, as described above.

However, to demonstrate the anisotropic RS characteristics according to the crystal orientation of the $CsPb_2Br_5$, the electronic structure and charge density of $CsPb_2Br_5$ were calculated using first-principle DFT [39]. Figure 7(d) shows the calculated electronic structure of bulk $CsPb_2Br_5$, and the calculated details can be found in the experimental section. Because the heavy metal Pb element is significantly affected by the spin-orbit coupling (SOC) effect, it was calculated in consideration of the SOC effect through the generalized gradient approximation Perdew–Burke–Ernzerhof (GGA-PBE) method [44, 45]. From this electronic structure, bulk $CsPb_2Br_5$ has an indirect bandgap of 2.39 eV, and has been underestimated compared to the actual bandgap as an inherent feature of GGA and SOC calculations [46, 47]. A low slope that is almost flat in the *A*-*M*, *Γ*-*Z*, and *R*-*X* directions and emphasized with reddish color indicates a very low group velocity of the electrons as a quasi-particle to those directions by the $V_{group}(k) = 1/\hbar[dE(k)/dk]$ relationship, which indicates that the interaction and electron movement between the (001) planes that were related to those directions are significantly restricted [48]. Conversely, owing to its relatively steep E-*k* slope in other directions, an interaction in those directions is permissible. These results indicate that the overall resistance of the planar-type device is significantly lower than that of the vertical-type device in the SC $CsPb_2Br_5$-based RS device with an inert electrode, which is free from the influence of active metal ions, as shown in Fig. 5(a). Meanwhile, the charge density in the conduction band minimum (CBM) is directly related to the carrier concentration, which is the number of electron charge carriers available for conduction [49]. Therefore, it is a crucial factor in predicting electrical properties. Figure 7(b) shows the electron charge density distribution in the (010) and (001) planes of the CBM (Γ-point). Notably, the charge-density distribution in the (001) plane of $CsPb_2Br_5$ was relatively uniform, whereas that in the (010) plane was strongly localized in each Cs layer. This suggests that there was little charge in the Cs layers, predominantly residing in the Pb_2Br_5 polyhedral layer. This phenomenon significantly hinders charge transport in the direction perpendicular to the (001) plane, which explains the extremely low HRS current in the vertical-type RS device. In contrast, the charge density was additionally calculated when Cu atoms were present in the Cs layer, which was

the most stable position revealed during the CI-NEB calculation process mentioned above. Figure 7(e) shows the calculated typical charge density distribution at the Γ-point caused by the Cu atom, which is present in the corresponding position. From the (010) plane view in Fig. 7(e), it is evident that a newly generated charge density around the Cu atom is present at the corresponding position, potentially facilitating restricted charge transport between the Cs layers.

Based on these theoretical and experimental analysis results, we suggest a possible mechanism for the observed RS behavior with voltage-driven multistate operation of an SC $CsPb_2Br_5$-based vertical-type device with a Cu TE, as shown in Fig. 8. In this description, only one CP was considered an effective explanation. The as-fabricated devices contained some intrinsic V_{Br} defects that were randomly distributed [13, 28, 50]. When a positive electric field is applied to the Cu TE, Cu^+ ions generated from the Cu TE at the interface between the Cu TE and SC $CsPb_2Br_5$ by a redox reaction can migrate toward the BE along the electric field, which corresponds to the direction perpendicular to the (001) plane. The migrated Cu^+ ions that are mostly present in the Cs layer, which were confirmed as the most stable state through CI-NEB calculations, were likely to be reduced around the Cs layer by electrons from the BE. The CPs formed in this manner eventually transitioned to the LRS state. The initial formation of CP required a high electric field owing to its passage through multiple Pb_2Br_5 layers oriented perpendicular to the (001) plane, which was associated with the high electrochemical forming voltage of the SC $CsPb_2Br_5$-based vertical-type device with a Cu TE. When a positive electric field was applied to the BE, the Cu atom was ionized again and migrated toward the TE. The electric field provided energy to ionize Cu and crossed the MBE of the Pb_2Br_5 layer depending on the strength of the electric field. Consequently, it induced partial annihilation of the CP, resulting in an SC $CsPb_2Br_5$-based vertical-type device with an active Cu TE that exhibited voltage-driven multistate characteristics. After the occurrence of this partial annihilation of CP, a significant number of Cu elements were already present throughout the Cs layers of $CsPb_2Br_5$, allowing the complete CP to be reformed with only a very low electric field applied to the TE.

Before concluding, a detailed comparison of previously reported inorganic bromidic-MHPs-based RS devices is provided in Table S1 in the ESM. It is clear that the SC $CsPb_2Br_5$-based RS device in this study has an improved on/off ratio and environmental stability, as well as a relatively low operating voltage (electric field), which is advantageous for implementing low-power operating memory devices. Furthermore, multi-level operation with large on/off ratio was achieved by adjusting the reset voltage rather than adjusting CC or using additional light irradiation, as seen in previous reports. This can facilitate the realization of multi-bit non-volatile storage system.

3 Conclusions

In conclusion, we successfully fabricated SC $CsPb_2Br_5$-based RS devices free from the influence of GBs with a high on/off resistance ratio (~ 10^8) and low operating voltage (< 0.32 V) in vertical-type structures. In addition, the fabricated device exhibited voltage-driven multistate characteristics with a substantially high resistance difference between each state (~ 10^2). Our study into the RS mechanism involved a comparative analysis of the RS characteristics across device structures (vertical and planar-type) and electrodes (inert and active), complemented by AES depth profiles and DFT with CI-NEB calculations. Our findings revealed that the main factor affecting the RS characteristics was the migration of active metal ions, which confirmed that the main causes of RS could strongly vary depending on the crystal structure. Furthermore, we identified the 2D structural features of alternatively stacked Cs layers, and the Pb_2Br_5 layer was the main reason for the multistate operation with a low operating voltage of the SC $CsPb_2Br_5$-based vertical-type RS device. These results complemented the current understanding that the movement of halogen defects such as halogen vacancies is the major cause of HP-based RS devices.

4 Experimental

4.1 Preparation of SC $CsPb_2Br_5$ MSs

SC $CsPb_2Br_5$ MSs were synthesized using a simple and environmentally friendly deionized (DI) water-based crystallization process, as shown in Fig. S1 in the ESM [21, 51]. At first, 0.025 M CsBr (99.999%, Sigma-Aldrich) and 0.05 M of $PbBr_2$ (99.998%, Sigma-Aldrich) were mixed in DI water in a vial. The temperature of the mixed solution was set at 90 °C under vigorous stirring. When the vial approached the set temperature and the solution became completely clear, it was removed from the double-boiler system and allowed to cool down naturally at ~ 25 °C without any stirring. After 35 min, a large number of $CsPb_2Br_5$ overgrown crystals sank to the bottom of the vial (labile zone), and a few $CsPb_2Br_5$ MSs started to form on the upper side of the solution (metastable zone). At this time, a portion of 150 μL of the up-side solution was quickly dropped on the prepared substrate to form a droplet-shaped growing zone. As shown in Fig. S13 in the ESM, particles grown in the metastable zone had a sheet shape without impurities, whereas those grown in the labile zone had

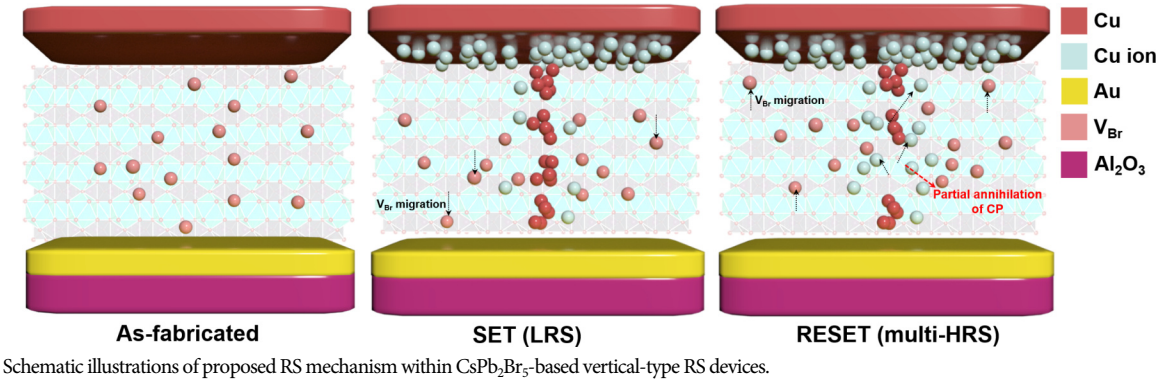

Figure 8 Schematic illustrations of proposed RS mechanism within $CsPb_2Br_5$-based vertical-type RS devices.

heterogeneous particles and shapes [52]. After a few minutes, when the micro-sized sheets grown in the solution were adhered to the substrate surface, the solution on the substrate was removed by N_2 blowing and briefly washed with anhydrous methyl alcohol (99.5%, Daejung) to remove impurities from the surface.

4.2 Fabrication of resistive switching devices

To fabricate vertical-type SC $CsPb_2Br_5$ MS-based RS devices, Au BE pre-patterned Al_2O_3 substrates were prepared using a thermal evaporation technique with a shadow mask. The $CsPb_2Br_5$ MSs were grown as described above. TE metals such as Cu, Au, and Ag were deposited by thermal evaporation with deposit rate of 0.3Å/s under ~ 10^{-6} torr vacuum level chamber using the same shadow mask rotated 90° horizontally. In the case of the planar type device, interdigitated type electrodes with an interval of about 2 μm were deposited on the cleaned Al_2O_3 substrates, through photolithography with 365 nm ultraviolet (UV) exposure, and lift-off processes. Finally, planar-type devices were fabricated by growing $CsPb_2Br_5$ MSs on an electrode-patterned substrate.

4.3 Characterizations and measurements

The surface morphology and thickness of the synthesized $CsPb_2Br_5$ MSs were measured using a field-emission scanning electron microscopy (FESEM; Verios G4 UC, FEI), an alpha step (Dektak XT, Bruker), and AFM (NX20, Park systems). The crystal structure was analyzed by XRD (Flex600, Bruker) with Cu Kα (λ = 1.5406 Å) and a HRTEM (JEM-2010, JEOL). Additionally, XRC was measured by HR-XRD (Xpert Pro, PANalytical) with Cu Kα (λ = 1.5406 Å). The Raman spectra of the synthesized $CsPb_2Br_5$ MSs were obtained using a micro-Raman spectrometer (DXR-3xi, Thermo Fisher Scientific). Elemental analysis of the synthesized materials was conducted using EDS using a SEM (SU-8010, Hitachi). The elemental depth profiles of the fabricated RS devices for each LRS and HRS state were measured using AES (PHI700Xi, Ulvac-phi). All the electrical characteristics were measured using a Keithley 2635b source meter module at room temperature and < 40% humidity.

4.4 Computational details

The plane wave method in the framework of the DFT as implemented in the Material Square was carried out using the Quantum ESPRESSO code [53]. The projected augmented wave (PAW) was used for describing interactions between the core and valence electron [54]. The GGA with the PBE functional was employed for the exchange-correlation effects, and the kinetic energy cut-off of the wave function was set to approximately 625 eV [55]. The non-defective super-cell, which consisted of a 2 × 1 × 2 repetition of a primitive unit cell with 64 atoms (8 formula units) of the tetragonal phase $CsPb_2Br_5$ was used for the electronic structure and ionic migration calculations. The cell parameters and atomic positions of all the structures were optimized with a convergence threshold of 1.3×10^{-5} eV. All atomic coordinates were fine-tuned, with a maximum force exerted on each atom below 0.02 eV/Å. Spin-orbit coupling was considered in the electronic structure calculations, including the band structure and electron charge density distribution. A calculation using the CI-NEB method was carried out to predict the ionic transitions along the minimum energy path with saddle points [56]. The alteration in the total charge within the system was taken into account, while spin-orbit coupling was not considered during the CI-NEB calculations.

Electronic Supplementary Material: Supplementary material (schematic illustrations of synthesis and fabrication process of $CsPb_2Br_5$ based RS devices, HRTEM analysis results, electrical characteristics of $CsPb_2Br_5$ based RS devices with different TE, cross-section SEM images of thin $CsPb_2Br_5$ based RS device, SEM images captured during ion etching with AES scanning, schematic illustration of specific Cu ion location in $CsPb_2Br_5$ cell with the most stable state, calculated MBEs of Ag ion in the $CsPb_2Br_5$, and optical images of being synthesized materials during the natural cooling process) is available in the online version of this article at https://doi.org/10.26599/NR.2025.94907023.

Data availability

All data needed to support the conclusions in the paper are presented in the manuscript and the Electronic Supplementary Material. Additional data related to this paper may be requested from the corresponding author upon request

Acknowledgements

This work was supported by the Institute of Information & Communications Technology Planning & Evaluation (IITP) under the Artificial Intelligence Semiconductor Support Program to Nurture Talent (IITP-(2024)-RS-2023–00253914) grant funded by the Korean government (MSIT).

Declaration of competing interest

All the contributing authors report no conflict of interests in this work.

Author contribution statement

U. J.: Investigation, data curation, formal analysis, investigation, methodology, software, validation, writing – original draft, and writing – review & editing. D.-S. W.: Formal analysis and validation. S. K.: Data curation and validation. Z. T.: Methodology and data curation. J. P.: Conceptualization, methodology, project administration, resources, supervision, validation, visualization, and writing – review & editing.

Use of AI statement

None.

References

[1] Choi, J.; Han, J. S.; Hong, K.; Kim, S. Y.; Jang, H. W. Organic–inorganic hybrid halide perovskites for memories, transistors, and artificial synapses. *Adv. Mater.* **2018**, *30*, 1704002.

[2] Ge, S. P.; Huang, Y. X.; Chen, X. J.; Zhang, X. R.; Xiang, Z. C.; Zhang, R. X.; Li, W. P.; Cui, Y. M. Silver iodide induced resistive switching in $CsPbI_3$ perovskite-based memory device. *Adv. Mater. Interfaces* **2019**, *6*, 1802071.

[3] Zhu, X. J.; Lee, J.; Lu, W. D. Iodine vacancy redistribution in organic–inorganic halide perovskite films and resistive switching effects. *Adv. Mater.* **2017**, *29*, 1700527.

[4] Xu, W. T.; Cho, H.; Kim, Y. H.; Kim, Y. T.; Wolf, C.; Park, C. G.; Lee, T. W. Organometal halide perovskite artificial synapses. *Adv. Mater.* **2016**, *28*, 5916–5922.

[5] Kim, S. G.; Van Le, Q.; Han, J. S.; Kim, H.; Choi, M. J.; Lee, S. A.; Kim, T. L.; Kim, S. B.; Kim, S. Y.; Jang, H. W. Dual-phase all-

inorganic cesium halide perovskites for conducting-bridge memory-based artificial synapses. *Adv. Funct. Mater.* **2019**, *29*, 1906686.
[6] Lao, J.; Xu, W.; Jiang, C. L.; Zhong, N.; Tian, B. B.; Lin, H. C.; Luo, C. H.; Travas-Sejdic, J.; Peng, H.; Duan, C. G. An air-stable artificial synapse based on a lead-free double perovskite $Cs_2AgBiBr_6$ film for neuromorphic computing. *J. Mater. Chem. C* **2021**, *9*, 5706–5712.
[7] Xu, J.; Wu, Y. H.; Li, Z. Z.; Liu, X. L.; Cao, G. Z.; Yao, J. X. Resistive switching in nonperovskite-phase $CsPbI_3$ film-based memory devices. *ACS Appl. Mater. Interfaces* **2020**, *12*, 9409–9420.
[8] Wu, Y.; Wei, Y.; Huang, Y.; Cao, F.; Yu, D. J.; Li, X. M.; Zeng, H. B. Capping $CsPbBr_3$ with ZnO to improve performance and stability of perovskite memristors. *Nano Res.* **2017**, *10*, 1584–1594.
[9] Liu, D. J.; Lin, Q. Q.; Zang, Z. G.; Wang, M.; Wangyang, P. H.; Tang, X. S.; Zhou, M.; Hu, W. Flexible all-inorganic perovskite $CsPbBr_3$ nonvolatile memory device. *ACS Appl. Mater. Interfaces* **2017**, *9*, 6171–6176.
[10] Shang, Y. Q.; Li, G.; Liu, W. M.; Ning, Z. J. Quasi-2D inorganic $CsPbBr_3$ perovskite for efficient and stable light-emitting diodes. *Adv. Funct. Mater.* **2018**, *28*, 1801193.
[11] Yuan, X.; Hou, X. M.; Li, J.; Qu, C. Q.; Zhang, W. J.; Zhao, J. L.; Li, H. B. Thermal degradation of luminescence in inorganic perovskite $CsPbBr_3$ nanocrystals. *Phys. Chem. Chem. Phys.* **2017**, *19*, 8934–8940.
[12] Guan, X. W.; Lei, Z. H.; Yu, X. C.; Lin, C. H.; Huang, J. K.; Huang, C. Y.; Hu, L.; Li, F.; Vinu, A.; Yi, J. B. et al. Low-dimensional metal-halide perovskites as high-performance materials for memory applications. *Small* **2022**, *18*, 2203311.
[13] Jung, J. H.; Kim, S. H.; Park, Y.; Lee, D.; Lee, J. S. Metal-halide perovskite design for next-generation memories: First-principles screening and experimental verification. *Adv. Sci.* **2020**, *7*, 2001367.
[14] Paul, T.; Sarkar, P. K.; Maiti, S.; Sahoo, A.; Chattopadhyay, K. K. Solution-processed light-induced multilevel non-volatile wearable memory device based on $CsPb_2Br_5$ perovskite. *Dalton Trans.* **2022**, *51*, 3864–3874.
[15] Li, H. B.; Wang, X. L.; Chu, H. Y.; Yao, X. D. High performance resistive memory device based on highly stable layered $CsPb_2Br_5$ perovskite polymer nanocomposite. *J. Alloys Compd.* **2022**, *921*, 166014.
[16] McGovern, L.; Koschany, I.; Grimaldi, G.; Muscarella, L. A.; Ehrler, B. Grain size influences activation energy and migration pathways in $MAPbBr_3$ perovskite solar cells. *J. Phys. Chem. Lett.* **2021**, *12*, 2423–2428.
[17] Park, Y.; Lee, J. S. Controlling the grain size of Dion-Jacobson-phase two-dimensional layered perovskite for memory application. *ACS Appl. Mater. Interfaces* **2022**, *14*, 4371–4377.
[18] Choi, J.; Park, S.; Lee, J.; Hong, K.; Kim, D. H.; Moon, C. W.; Park, G. D.; Suh, J.; Hwang, J.; Kim, S. Y. et al. Organolead halide perovskites for low operating voltage multilevel resistive switching. *Adv. Mater.* **2016**, *28*, 6562–6567.
[19] Qin, C. J.; Matsushima, T.; Sandanayaka, A. S. D.; Tsuchiya, Y.; Adachi, C. Centrifugal-coated quasi-two-dimensional perovskite $CsPb_2Br_5$ films for efficient and stable light-emitting diodes. *J. Phys. Chem. Lett.* **2017**, *8*, 5415–5421.
[20] Lin, C. J.; Liu, L.; Xu, J. Z.; Fang, F. E.; Jiang, K.; Liu, Z. X.; Wang, Y.; Chen, F. M.; Yao, H. Z. Facile synthesis of a dual-phase $CsPbBr_3$-$CsPb_2Br_5$ single crystal and its photoelectric performance. *RSC Adv.* **2020**, *10*, 20745–20752.
[21] Zhang, Z. J.; Zhu, Y. M.; Wang, W. L.; Zheng, W.; Lin, R. C.; Huang, F. Growth, characterization and optoelectronic applications of pure-phase large-area $CsPb_2Br_5$ flake single crystals. *J. Mater. Chem. C* **2018**, *6*, 446–451.
[22] Feng, X. L.; Zhang, L.; Zhang, B. B.; You, J. X.; Li, K.; Zeng, H. Q.; Wang, X. F.; Dai, Z. H.; Jia, S. L.; Bao, H. B. et al. Ligand-assisted growth of 2D perovskite single crystal for highly sensitive X-ray detectors. *Adv. Funct. Mater.*, in press, https://doi.org/10.1002/adfm.202402166.
[23] Zhang, M. Z.; Zheng, Z. P.; Fu, Q. Y.; Chen, Z.; He, J. L.; Zhang, S.; Yan, L.; Hu, Y. X.; Luo, W. Growth and characterization of all-inorganic lead halide perovskite semiconductor $CsPbBr_3$ single crystals. *CrystEngComm* **2017**, *19*, 6797–6803.
[24] Zhang, L. Q.; Yang, X. L.; Jiang, Q.; Wang, P. Y.; Yin, Z. G.; Zhang, X. W.; Tan, H. R.; Yang, Y.; Wei, M. Y.; Sutherland, B. R. et al. Ultra-bright and highly efficient inorganic based perovskite light-emitting diodes. *Nat. Commun.* **2017**, *8*, 15640.
[25] Marques, A. S.; Faria, R. M.; Freitas, J. N.; Nogueira, A. F. Low-temperature blade-coated perovskite solar cells. *Ind. Eng. Chem. Res.* **2021**, *60*, 7145–7154.
[26] Hua, J. C.; Deng, X.; Niu, C.; Huang, F. Z.; Peng, Y.; Li, W. N.; Ku, Z. L.; Cheng, Y. B. A pressure-assisted annealing method for high quality $CsPbBr_3$ film deposited by sequential thermal evaporation. *RSC Adv.* **2020**, *10*, 8905–8909.
[27] Wang, R. D.; Li, Z.; Li, S. T.; Wang, P. F.; Xiu, J.; Wei, G. X.; Liu, H. Q.; Jiang, N.; Liu, Y. Y.; Zhong, M. Z. All-inorganic perovskite $CsPb_2Br_5$ nanosheets for photodetector application based on rapid growth in aqueous phase. *ACS Appl. Mater. Interfaces* **2020**, *12*, 41919–41931.
[28] Yin, J.; Yang, H. Z.; Song, K. P.; El-Zohry, A. M.; Han, Y.; Bakr, O. M.; Brédas, J. L.; Mohammed, O. F. Point defects and green emission in zero-dimensional perovskites. *J. Phys. Chem. Lett.* **2018**, *9*, 5490–5495.
[29] Dellinger, J. H. *The Temperature Coefficient of Resistance of Copper*; Govt. Print. Off.: Washington, 1911.
[30] Munjal, S.; Khare, N. Advances in resistive switching based memory devices. *J. Phys. D: Appl. Phys.* **2019**, *52*, 433002.
[31] Zhang, Y.; Wu, H. Q.; Bai, Y.; Chen, A.; Yu, Z. P.; Zhang, J. Y.; Qian, H. Study of conduction and switching mechanisms in $Al/AlO_x/WO_x/W$ resistive switching memory for multilevel applications. *Appl. Phys. Lett.* **2013**, *102*, 233502.
[32] Minnekhanov, A. A.; Shvetsov, B. S.; Martyshov, M. M.; Nikiruy, K. E.; Kukueva, E. V.; Presnyakov, M. Y.; Forsh, P. A.; Rylkov, V. V.; Erokhin, V. V.; Demin, V. A. et al. On the resistive switching mechanism of parylene-based memristive devices. *Org. Electron.* **2019**, *74*, 89–95.
[33] Fan, Y.; King, S. W.; Bielefeld, J.; Orlowski, M. K. Characterization of porous BEOL dielectrics for resistive switching. *ECS Trans.* **2016**, *72*, 35.
[34] Ghosh, G.; Kang, Y.; King, S. W.; Orlowski, M. Role of CMOS back-end metals as active electrodes for resistive switching in ReRAM cells. *ECS J. Solid State Sci. Technol.* **2017**, *6*, N1–N9.
[35] Sun, Y. M.; Tai, M. Q.; Song, C.; Wang, Z. Y.; Yin, J.; Li, F.; Wu, H. Q.; Zeng, F.; Lin, H.; Pan, F. Competition between metallic and vacancy defect conductive filaments in a $CH_3NH_3PbI_3$-based memory device. *J. Phys. Chem. C* **2018**, *122*, 6431–6436.
[36] Sun, Y. M.; Song, C.; Yin, S. Q.; Qiao, L. L.; Wan, Q.; Wang, R.; Zeng, F.; Pan, F. Design of a controllable redox-diffusive threshold switching Memristor. *Adv. Electron. Mater.* **2020**, *6*, 2000695.
[37] Ali, A.; Abbas, H.; Hussain, M.; Jaffery, S. H. A.; Hussain, S.; Choi, C.; Jung, J. Thickness-dependent monochalcogenide GeSe-based CBRAM for memory and artificial electronic synapses. *Nano Res.* **2022**, *15*, 2263–2277.
[38] Su, T. K.; Cheng, W. K.; Chen, C. Y.; Wang, W. C.; Chuang, Y. T.; Tan, G. H.; Lin, H. C.; Hou, C. H.; Liu, C. M.; Chang, Y. C. et al. Room-temperature fabricated multilevel nonvolatile lead-free cesium halide memristors for reconfigurable in-memory computing. *ACS Nano* **2022**, *16*, 12979–12990.
[39] Lee, M. J.; Kim, S. H.; Lee, S.; Yoon, C.; Min, K. A.; Choi, H.; Hong, S.; Lee, S.; Park, J. G.; Ahn, J. P. et al. Understanding filamentary growth and rupture by Ag ion migration through single-crystalline 2D layered $CrPS_4$. *NPG Asia Mater.* **2020**, *12*, 82.
[40] Oranskaia, A.; Yin, J.; Bakr, O. M.; Brédas, J. L.; Mohammed, O. F. Halogen migration in hybrid perovskites: The organic cation matters. *J. Phys. Chem. Lett.* **2018**, *9*, 5474–5480.
[41] Gala, D. K.; Sharma, A. A.; Li, D. S.; Goodwill, J. M.; Bain, J. A.;

Skowronski, M. Low temperature electroformation of TaO_x-based resistive switching devices. *APL Mater.* **2016**, *4*, 016101.
[42] Ielmini, D.; Nardi, F.; Cagli, C.; Lacaita, A. L. Size-dependent retention time in NiO-based resistive-switching memories. *IEEE Electron Device Lett.* **2010**, *31*, 353–355.
[43] Qi, M.; Bai, L.; Xu, H. Y.; Wang, Z. Q.; Kang, Z. H.; Zhao, X. N.; Liu, W. Z.; Ma, J. G.; Liu, Y. C. Oxidized carbon quantum dot-graphene oxide nanocomposites for improving data retention of resistive switching memory. *J. Mater. Chem. C* **2018**, *6*, 2026–2033.
[44] Even, J.; Pedesseau, L.; Jancu, J. M.; Katan, C. Importance of spin-orbit coupling in hybrid organic/inorganic perovskites for photovoltaic applications. *J. Phys. Chem. Lett.* **2013**, *4*, 2999–3005.
[45] Stroppa, A.; Di Sante, D.; Barone, P.; Bokdam, M.; Kresse, G.; Franchini, C.; Whangbo, M. H.; Picozzi, S. Tunable ferroelectric polarization and its interplay with spin-orbit coupling in tin iodide perovskites. *Nat. Commun.* **2014**, *5*, 5900.
[46] Du, M. H. Efficient carrier transport in halide perovskites: Theoretical perspectives. *J. Mater. Chem. A* **2014**, *2*, 9091–9098.
[47] Xu, Z. W.; Zhang, C. R.; Wu, Y. Z.; Gong, J. J.; Wang, W.; Liu, Z. J.; Chen, H. S. Density functional theory study on the electronic structures and related properties of Ag-doped $CH_3NH_3PbI_3$ perovskite. *Results Phys.* **2019**, *15*, 102709.
[48] Brillouin, L. *Wave Propagation in Periodic Structures: Electric Filters and Crystal Lattices*, 2nd ed.; Dover Publications: New York, 1953.
[49] Ning, H. L.; Liu, X. Z.; Ruan, H. G.; Peng, C.; Huang, F. X.; Deng, Y. X.; Yuan, W. J.; Yao, R. H.; Qiu, B.; Wang, X. F. Density functional theory study of the electronic and optical properties of Si incorporated SnO_2. *AIP Adv.* **2019**, *9*, 115104.
[50] Liu, Z. F.; Peters, J. A.; Pan, L.; Klepov, V.; De Siena, M.; Benadia, A.; Chung, D. Y.; Kanatzidis, M. G.; Wessels, B. W. Investigation of defects in melt and solution grown perovskite $CsPbBr_3$ single crystals. *Appl. Phys. Lett.* **2023**, *122*, 131902.
[51] Yin, J.; Zhang, G. D.; Tao, X. T. A fractional crystallization technique towards pure mega-size $CsPb_2Br_5$ single crystal films. *CrystEngComm* **2019**, *21*, 1352–1357.
[52] Sudha, C.; Srinivasan, K. Supersaturation dependent nucleation control and separation of mono, ortho and unstable polymorphs of paracetamol by swift cooling crystallization technique. *CrystEngComm* **2013**, *15*, 1914–1921.
[53] Giannozzi, P.; Baroni, S.; Bonini, N.; Calandra, M.; Car, R.; Cavazzoni, C.; Ceresoli, D.; Chiarotti, G. L.; Cococcioni, M.; Dabo, I. et al. Quantum Espresso: A modular and open-source software project for quantum simulations of materials. *J. Phys.: Condens. Matter* **2009**, *21*, 395502.
[54] Kresse, G.; Joubert, D. From ultrasoft pseudopotentials to the projector augmented-wave method. *Phys. Rev. B* **1999**, *59*, 1758–1775.
[55] Perdew, J. P.; Burke, K.; Ernzerhof, M. Perdew, burke, and ernzerhof reply. *Phys. Rev. Lett.* **1998**, *80*, 891.
[56] Henkelman, G.; Uberuaga, B. P.; Jónsson, H. A climbing image nudged elastic band method for finding saddle points and minimum energy paths. *J. Chem. Phys.* **2000**, *113*, 9901–9904.